

Detection of Landslide Areas Using Satellite Radar Interferometry

Hiroshi Kimura and Yasushi Yamaguchi

Abstract

Three interferograms constructed from JERS-1 SAR data collected from June to October, 1995 were used to analyze the Itaya landslide in Japan by the three-pass method and the digital elevation model elimination (DEME) method. The differential interferograms produced by the three-pass method indicate only the extent of the displacement field, and fine geometrical features can not be recovered. In contrast, those produced by the DEME method indicate the different mechanical behaviors of the displacement from June to September and September to October, suggesting the existence of several sub-blocks in the landslide and the combination of irregular sub-block movements and steady-state movement of the entire block. The interferograms and the precipitation record allow us to construct a preliminary model with sub-block movements along shallow slip planes during a larger precipitation period and steady-state movement of the major landslide block along the deep arcuate slip plane. SAR interferometry can reveal the behavior of the landslide that could not be observed with the discrete GPS measurements of July to October, 1996.

Introduction

Mapping of coseismic displacement fields using differential satellite radar interferometry (Gabriel *et al.*, 1989) was first demonstrated by Massonnet *et al.* (1993) and Zebker *et al.* (1994). In addition, satellite radar interferometry was applied to monitor volcanic activity by Massonnet *et al.* (1995) and ice sheet flow by Goldstein *et al.* (1993). Researchers are now seeking other fields in which satellite radar interferometry might be applied. Landslide hazard detection is one of great social concern. Therefore, the authors have applied satellite interferometry to landslide detection.

Landslide areas are generally smaller than areas affected by earthquakes or volcanic activity, and are divided into two types: progressive and sporadic. Sporadic landslides, from which large deformations generally result in a short period, are difficult to measure. However, small progressive slips are often likely to occur prior to a sporadic slip. Therefore, progressive slips are investigated in order to enhance disaster prevention capabilities. Satellite radar interferometry in conjunction with external digital elevation models (DEMs) can be used to detect large fields of displacement (Massonnet *et al.*, 1993). This method, the Digital Elevation Model Elimination (DEME) method, uses external DEMs to remove topographic effects in a radar interferogram (Massonnet *et al.*, 1996). In addition, Zebker *et al.* (1994) have demonstrated that the multi-pass

method is capable of detecting coseismic fields, and Kwok *et al.* (1996) and Joughin *et al.* (1998) applied the multi-pass method to detect the Greenland ice stream. The multi-pass method requires no DEM, because topography can be determined from its own interferometric data.

Fruneau *et al.* (1996) observed and modeled the "La Clapiere" landslide in southeast France. ERS-1 synthetic aperture radar (SAR) interferograms indicated steady-state displacement over 12 days, but a non-uniform displacement gradient from top-to-bottom. The same area was studied by Carnec *et al.* (1996) using the same ERS-1 SAR interferometric combinations. Although the data were in good agreement with conventional data, they concluded that differential SAR interferometry is not suitable for applications involving high deformation gradients associated with short-time evolution on steeply sloping terrain. Both of these studies used data from ERS-1 with a three-day repeat cycle and the DEME method.

In this paper, the Itaya landslide is analyzed using three interferograms produced over a 132-day period from 09 June to 19 October, 1995 from JERS-1 L-band (23.5-cm wavelength) SAR data. Both the three-pass method and the DEME method were applied. The objective of this study was to analyze the landslide by SAR interferometry and to compare the three-pass and DEME methods for studying the landslide. First, the Itaya landslide is described. Then, the dataset and precipitation record used to study the landslide are shown, and the respective procedures used in these two methods to form the differential interferograms are described. Next, the differential interferograms and their respective analyses are described, and the models constructed based on the interferograms are discussed. Finally, conclusions are presented.

Study Site

The test site selected for this study is an active landslide in the Itaya area (38° 48' and 140° 16' E), Yamagata Prefecture, northern Japan. According to the local people, the landslide has been active since the early 1990s. Field surveys were carried out in the fall of 1994, the summer and fall of 1996, and the fall of 1997. The landslide is located on the northern slope of the Azumayama Volcano, which is a Quaternary andesitic strato-volcano having a summit elevation of 1,949 m. Geologically, the surface of the landslide and its surrounding areas is covered by debris flow deposits composed of andesitic volcanic rocks of the Azumayama Volcano. Sedimentary and volcanic rocks of Neogene Tertiary can be observed along major streams in this area and are overlain by the debris flow deposits. A large portion of the Neogene formations is hydrothermally altered to

K. Kimura is with the Department of Electrical and Electronic Engineering, Gifu University, 1-1 Yanagido, Gifu-shi 501-1193, Japan (hkimura@cc.gifu-u.ac.jp).

Y. Yamaguchi is with the Department of Earth and Planetary Sciences, Graduate School of Science, Nagoya University, Furo-cho, Chikusa-ku, Nagoya 464-8602, Japan (yasushi@eps.nagoya-u.ac.jp).

Photogrammetric Engineering & Remote Sensing
Vol. 66, No. 3, March 2000, pp. 337-344.

0099-1112/00/6503-337\$3.00/0

© 2000 American Society for Photogrammetry
and Remote Sensing

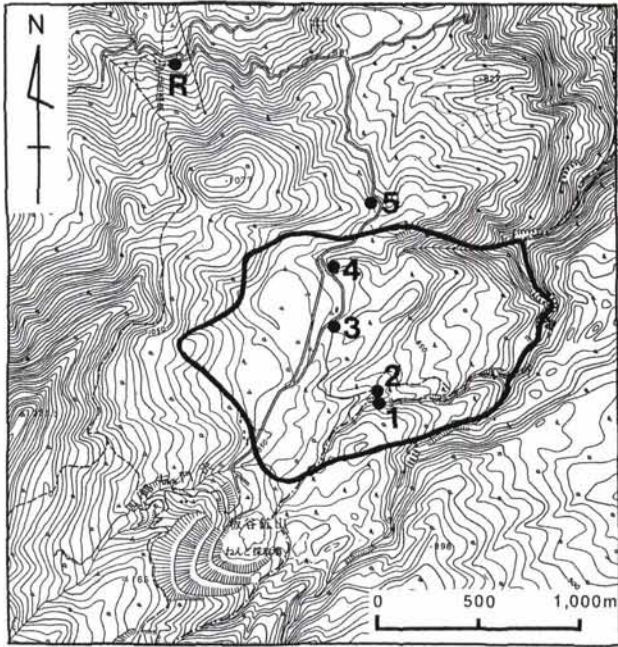


Figure 1. Outline of the Itaya landslide, Yamagata Prefecture, Japan. Numbers 1 to 5 indicate the locations of the GPS measurements used to detect landslide movement, and **R** indicates the immovable reference point (modified from Fujii *et al.* (1997)).

form clay minerals. An abandoned kaolinite mine pit lies adjacent (southwest) to the landslide block.

As shown in Figure 1, the landslide—approximately 1 km wide (north-south) and 2 km long (east-west)—is rectangular

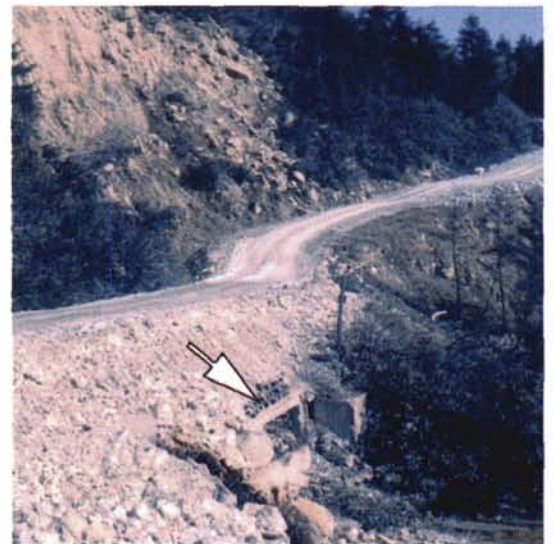
in shape and is moving eastward. The outline of the landslide block was drawn by field observations and photogeologic interpretations of SPOT HRV and ADEOS AVNIR images (Yamaguchi *et al.*, 1999). A head crown is easily recognizable at the western boundary of the landslide at elevations of about 950 m to 1,020 m. The northern rim of the landslide is also clear, and is defined by cliffs with fresh rock and soil surfaces. However, the western half of the southern rim is unclear topographically, because the surface in that area is relatively flat and is covered with thick debris flow deposits. The eastern half probably lies along a stream, as shown in Figure 1. The landslide toe in the east extends to a stream at elevations of 670 m to 850 m. The main slip plane of the landslide is probably located at the boundary between the Quaternary debris flow deposits and the hydrothermally altered Neogene rocks, or in the Neogene formations. Inside the main block, sub-blocks of smaller landslides are found, the slip planes of which are shallower than the main slip plane.

Plates 1a and 1b are ground photographs viewed from the northern rim of the landslide along the road between points #4 and #5. Plate 1a is a view to the southwest, in which the relatively flat bare soil area is sliding down toward the left (east), and the surrounding stable surfaces are covered with trees. Plate 1b is a view to the northwest which shows subsidence of the previous road surface where an underdrain (arrow in Plate 1b) is located. Based upon field observations in 1994, 1996, and 1997, new bare rock and soil surfaces without vegetation cover are being generated due to landslide movement in the crown and marginal areas. Small scale rapid flows can be observed on the head and side scarps. The toe area of the landslide is approximately 100 to 200 m wide, and is divided by many local longitudinal and transverse fractures into small sub-blocks, which are rotated to various directions, and are eventually slumped into the stream as chaotic mud flows.

The landslide movement was measured by a differential GPS technique in July and October 1996 (Fujii *et al.*, 1997). Figure 1 shows the locations of the GPS measurements. An immobile reference point (**R** in Figure 1) is located at Goshiki Hot Springs about 1 km north of the landslide, where GPS signals were continuously monitored for a few days. Five measurement points, both inside



(a)



(b)

Plate 1. Ground photographs of the Itaya landslide from a position between #4 and #5 shown in Figure 1. Views are to the southwest (a) and to the northwest (b). An underdrain below the surface of the road (arrow) indicates subsidence.

TABLE 1. DISPLACEMENT RATE AND DIRECTION OF THE LANDSLIDE MOVEMENT MEASURED IN JULY AND OCTOBER, 1996 BY THE DIFFERENTIAL GPS TECHNIQUE (FUJII *ET AL.*, 1997). THE DIRECTION IS INDICATED BY DEGREES MEASURED CLOCKWISE FROM NORTH

Point #	Measured Displacement (m)		Displacement Rate (mm/day)	Direction (degrees)
	(E-W)	(N-S)		
1	0.078	-0.004	1.1	93
2	0.495	0.029	6.9	87
3	0.738	0.057	10.3	86
4	0.769	0.096	10.8	83
5	-0.003	0.004	0.07	-37

and outside of the landslide block, were selected. GPS data were collected over approximately 4 to 6 hours at each measurement point. The reference data were collected continuously at point R. These GPS measurements were carried out on 30 July and 10 October 1996. Total displacements over the period between these two dates, 72 days, are shown in Table 1. Point #1 is located at a concrete bank along a stream. Point #2 is located approximately 50 m north and 20 m higher than point #1. The landslide block is locally collapsed into the stream near point #1, where the displacement is much smaller than at point #2. More specifically, point #1 is located below or very close to the main slip plane, and point #2 is located in the landslide block. Judging from the displacements of these two points and field observations, the slip plane is probably located between points #1 and #2. Points #3 and #4 indicate similar displacement rates and directions, that is, approximately 1 cm per day eastward. Point #5 shows a very small displacement, because this point is located outside of the landslide block.

This area is usually covered with snow from December to March, when the landslide is likely to be relatively inactive due to low temperatures and the consequent shortage of surface and shallow liquid water. Generally, landslide movement is the most active during the snow melting season and the subsequent rainy season, from April to August in this particular area. However, from September to November, landslide movement generally becomes steady-state due to moderate precipitation and temperature, although the authors have not actually recorded monitoring data continuously throughout a year.

Therefore, we assume that the GPS measurements from July to October 1996 (Fujii *et al.*, 1997) represent the average movements of this landslide from June to November.

Data Selection

More than 20 images covering the landslide were acquired by the JERS-1 L-band SAR with a 44-day repeat cycle from 1994 to 1996. Three sets of data obtained on 09 June, 05 September, and 19 October in 1995 were selected based on a rough estimate of baseline distances from satellite orbit data. Among the images observed from July to October 1996, when the GPS measurements were conducted, no combination was found to have a sufficiently short baseline and elapsed time.

The raw signal data were correlated to single-look complex images using the frequency domain convolution algorithm (Curlander and McDonough, 1991). The coregistration of the images was performed by maximizing the correlation between the two images at 3 by 3 tie-points distributed at identical intervals over approximately 60 km in azimuth and 75 km in range. The geometric deformation between the two images is corrected by resampling one image using second-order polynomials to match tie-point positions. However, an accurate baseline at the centimeter level is necessary in order to remove the spherical-Earth surface phase (flatten phase) and/or simulate the topographic phase for the three-pass method and the DEM method. The orbit data of JERS-1 does not allow such accuracy (Fujiwara *et al.*, 1998). Baselines of the three interferometric pairs were estimated using the unwrapped phase, with 11 ground reference points (GRPs) over the scene (Kimura and Todo, 1997). In baseline estimation, GRP elevations above sea level are placed on a sphere whose radius is based on the WGS-84 Earth ellipsoid model and the geodetic latitude of the scene center. The difference between ellipsoid height and geoid height is 41 m to 42 m over the scene. However, this difference was not considered, and that did not cause any problems in the following procedures. Three flattened interferograms, low-pass-filtered 15-look in range by 45-look in azimuth (200 m square), and a SAR backscatter image are shown in Plates 2a to 2d. These interferograms cover about 15 km in azimuth by 12 km in range, including the landslide (circled), and are presented in the slant-range format. The June to September and June to October interferograms (Plates 2a and 2d) have similar fringe intervals with reverse color change, because normal baselines have almost the same absolute value, but opposite

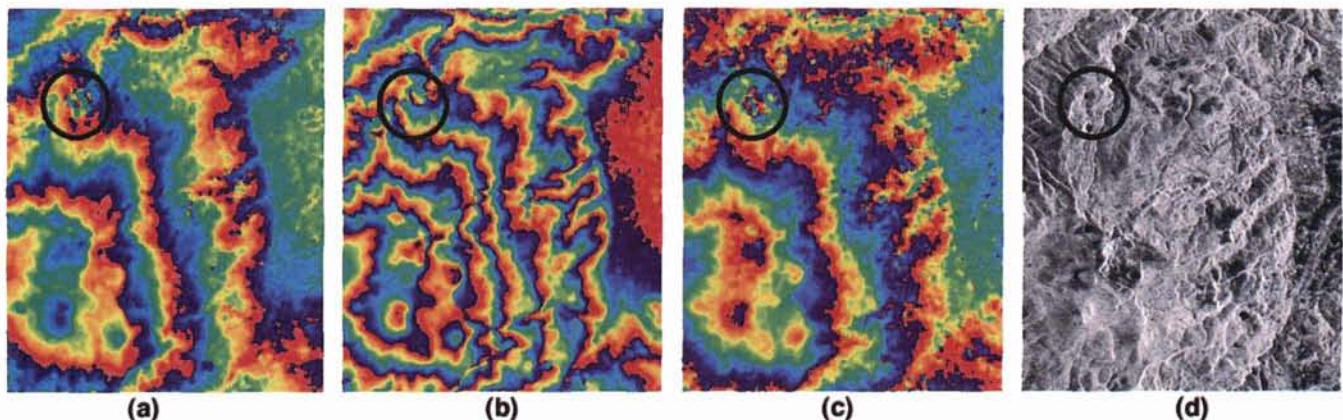


Plate 2. Flattened interferograms and backscatter image of the 15-km by 12-km area, including the landslide (circled) in slant range format. (a) June to September—altitude of ambiguity: -500 m. (b) September to October—altitude of ambiguity: 278 m. (c) June to October—altitude of ambiguity: -631 m. (d) Backscatter amplitude.

sign. The signal-to-noise ratio (SNR) of the June to October interferogram (Plate 2d) is lowest, presumably due to the longest elapsed time (133 days).

The Washikura station of the Automated Meteorological Data Acquisition System (AMEDAS), operated by the Japan Meteorological Agency, is located about 10 km south of the landslide at almost the same elevation. The weather during SAR data acquisition was cloudy on all three days. On 09 June, precipitation of 1 mm was recorded five hours before SAR data acquisition. Precipitation was less than 1 mm during the 48 hours before SAR data acquisition on both 09 September and 15 October. The September to October interferogram (Plate 2b), obtained over a short time interval (44 days) and under little precipitation, provides clear fringes. Monthly precipitation records at the Washikura station in 1995 (Figure 2) shows a high degree of precipitation from June to August and a much lower degree from September to October in these areas.

All JERS-1 images used in this paper were acquired from descending orbits, and therefore are taken from the east south-east direction. A full phase change (2π) is equivalent to a displacement of 11.8 cm along the line-of-sight of the radar, or 5.9 cm along the landslide average slope with 10° inclination and eastward direction. Given the displacement of 1 cm/day along the slope, the average deformation observed by the radar over 44 days will be 14.9π . In reality however, the phase of an interferogram is only modulo 2π ; therefore, the actual value will be 0.9π and the fringes should be traced (or unwrapped) from surrounding immovable areas in order to obtain the absolute value, 14.9π in this case.

Differential Interferogram Production

Three-pass method

The interferometric fringes shown in Plate 2 indicate the effects of both topography and the landslide. Phase variations are observed within the circle in Plates 2a to 2c, but the contribution of topography should be eliminated in order to detect only the landslide. This approach is based on that employed by Kwok *et al.* (1996) to measure the relative velocities of the ice stream. The landslide velocity is assumed to be constant over time.

The three images are referred to by their order of acquisition in a 44-day repeat cycle: 0 (09 June 1995), 2 (05 September

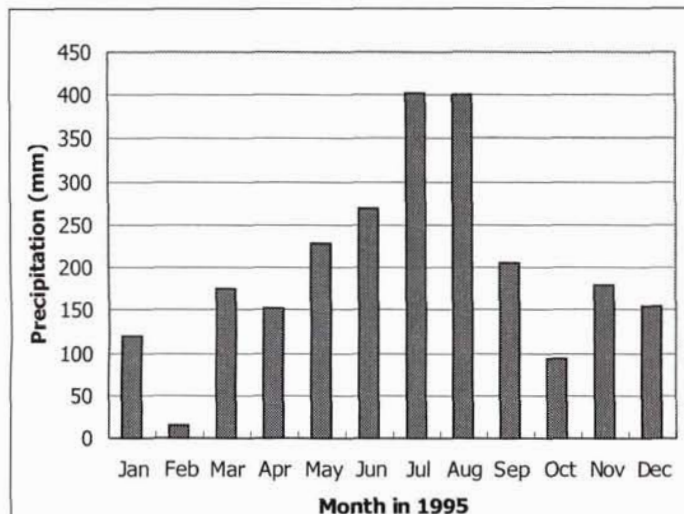


Figure 2. Precipitation in 1995 at Washikura, located 10 km south of the landslide. The data were collected by the Automated Meteorological Data Acquisition System (AMEDAS) of the Japan Meteorological Agency.

1995) and 3 (19 October 1995). Under the assumption of constant movement, the interferometric phase from the combination of image-*i* and image-*j* over the displacement feature is

$$\phi_{ij} = c_{ij}h + (j - i)\Delta\phi_d \quad (1)$$

where *h* is topographic height, $\Delta\phi_d$ is the phase due to displacement during one observation period (44 days), and c_{ij} , the factor of height to phase, is given by

$$c_{ij} = \frac{4\pi R_e B_{ij\perp}}{\lambda R(R_e + H) \sin \theta} \quad (2)$$

where B_{\perp} is the perpendicular component of the baseline (Table 2), R_e is the radius of the Earth ellipsoid curvature, *R* is the slant range distance, *H* is radar altitude, and θ is the off-nadir angle of slant range. The displacement distance in slant range during one observation period is

$$\Delta\rho_0 = \frac{\lambda}{4\pi} \Delta\phi_d \quad (3)$$

where λ is the radar wavelength (24 cm in this study). The interferometric phases of June to September, September to October, and June to October are expressed as ϕ_{02} , ϕ_{23} , and ϕ_{03} . From the combination of ϕ_{02} and ϕ_{23} , the contributions of the displacement and the height can be derived from Equations 1 and 2, if the topographic change is small enough compared to the ambiguity height: i.e.,

$$\Delta\phi_d = \frac{c_{23}\phi_{02} - c_{02}\phi_{23}}{2c_{23} - c_{02}} \quad (4)$$

$$h = \frac{2\phi_{23} - \phi_{02}}{2c_{23} - c_{02}} \quad (5)$$

Similarly, from the combinations (ϕ_{02} , ϕ_{03}) and (ϕ_{23} , ϕ_{03}), the respective contributions of displacement and height can be derived.

Phases ϕ_{02} , ϕ_{23} , and ϕ_{03} are unwrapped before applying Equation 4. Several methods for phase unwrapping have been developed. In this study, the method based on a branch cut algorithm (Goldstein *et al.*, 1988) is used. Only the area shown in Plate 2 was unwrapped. The area for unwrapping was limited in order to minimize error propagation. If residues are connected by incorrect branch cuts, phase unwrapping errors are propagated from there. The selected area includes the landslide having high coherence and low density of residues.

DEME Method

Using the Geographical Survey Institute of Japan 50-m grid DEM, the estimated baseline and the orbit data of the master image, the interferometric phase, and radar backscatter images are simulated. A slight mismatch in pixel position was observed between the simulation image and the real image due to the error of the absolute orbit position. The radar backscatter simulation image was used to co-register the simulated interferometric phase and the interferogram. Several tie points were selected on the radar backscatter simulation and real images;

TABLE 2. ESTIMATED NORMAL BASELINE (IN METERS) AT THE STUDY AREA OF THREE INTERFEROMETRIC PAIRS

	05 September	19 October
09 Jan.	-109.4	101.6
05 September		210.9

then the affine transformation was applied. Mismatch in range direction was too small to produce geometric errors in simulation due to a slight change of the incidence angle. To remove the topographic contributions, the simulated and coregistered interferometric phase was subtracted from the observed interferogram (not unwrapped).

Interferogram Production

Plate 3 displays the five geocoded differential interferograms and the radar backscatter image corresponding to the area shown in Figure 1. Limits of the landslide from the ground survey and locations of GPS measurements in Figure 1 are overlaid on the five interferograms. The map of Figure 1 super-imposed on the radar backscatter image indicates the geometric accuracy of these interferograms. The end of the landslide toe and the mine pit southwest of the landslide appear in the correct position in the backscatter image.

Interferogram Analysis

Plates 3a to 3c are interferograms produced by the three-pass method assuming a constant displacement velocity, and Plates 3d and 3e are those produced by the DEME method. All five interferograms reveal the phase variations associated with the landslide. Plate 3a shows the mean phase change during one observation period ($\Delta\phi_d$) from the three combinations (ϕ_{02} , ϕ_{23}), (ϕ_{02} , ϕ_{03}), and (ϕ_{23} , ϕ_{03}). Each flattened phase ϕ was filtered 15-look by 45-look (200-m square) before phase unwrapping. Only two of the three interferometric phases, ϕ_{02} , ϕ_{23} , and ϕ_{03} (Plates 2a to 2c), are independent, and because one can be derived from the others, the three displacement phases must be dependent. This is true at the stage before low-pass-filtering and unwrapping. However, separate filtering and unwrapping of ϕ_{02} , ϕ_{23} , and ϕ_{03} decreases the dependency among the three interferometric phases. In Plate 3a, negative phase variations can be detected in only the west half of the landslide. The phase changes are -0.5π to -0.8π , corresponding to a movement of 0.3 mm/day to 0.4 mm/day along the average slope. These values are smaller than the expected value described earlier in the Data Selection section. Plate 3b shows the phase changes over one observation period ($\Delta\phi_d$) from the combination of ϕ_{02} and ϕ_{23} , which shows the higher SNR in Plate 2. In order to preserve the detailed features of the interferogram, a smaller filter of 11-look by 33-look (150-m square) was used before unwrapping. In Plate 3b, the phase variations can be easily detected in the east half of the landslide; however, phase discontinuities are also found in this area. These are attributed to incorrect cuts connecting residues in phase unwrapping. These incorrect cuts suggest the presence of fast or chaotic motion. Residues caused by noise can be reduced by using a larger filter; however, some real features in the interferogram could be lost. A large filter is not always efficient for analysis of the landslide, as shown in Plate 3b. Cuts will change among different interferometric pairs and among those filtered using a different window size. Therefore, filtering respective interferograms with a larger filter and averaging the unwrapped phases smooths out phase variations, as shown in Plate 3a. The phase change shown in Plate 3b is rescaled by a factor of 2 (Plate 3c) and can be compared with the phase change during two observation periods ($2\Delta\phi_d$). In Plates 3b and 3c, the geometry of the fringes in the east half of the landslide can not be recovered, suggesting the inability to unwrap the phase within the landslide. The phase changes of the west half of the landslide, shown in Plate 3b, are -1.2π to -0.5π , corresponding to movements of 0.3 mm/day and 0.6 mm/day along the average slope. These values are still smaller than those expected.

Plates 3d and 3e display the June to September and September to October interferograms filtered 11-look by 33-look (150-m square) by the DEME method. However, phase variations

associated with the landslide are provided in both interferograms. Fringe patterns and their extents are significantly different between these two interferograms, even if we consider the difference in elapsed time (88 days and 44 days). The fringes of the June to September interferogram (Plate 3d) are too complicated to allow the geometry to be recovered; however, this seems to indicate the presence of several small sub-blocks in the major landslide block. In Table 1, the GPS displacement at point #2 is considerably different from those at points #3 and #4. Therefore, point #2 is probably located in a different sub-block than that of points #3 and #4. Points #3 and #4 show quite similar displacements. Because these two points are in very close interference phases in Plate 3d, points #3 and #4 are very likely located in the same sub-block. The fringes of Plate 3d also look similar to those over the two observation periods obtained by the three-pass method (Plate 3c) except for areas affected by errors of residue connections, suggesting that dominant deformation from June to October occurred from June to September. The complicated fringes in Plate 3d suggest a disrupted deformation and/or high deformation gradients, which may have caused the cut errors shown in Plates 3b and 3c.

In contrast, the fringes of the September to October interferogram (Plate 3e) are rather simple. In this interferogram, the phase change can not be detected in the southwestern part of the landslide. The differences in the fringe systems shown in Plates 3d and 3e also suggest the existence of different blocks within the landslide. In the September to October interferogram (Plate 3e), the phase changes in the central part having a height ranging from 800 m to 940 m is closely related to the topographic height. A positive phase rotation from the lower part to the upper part corresponds to a positive displacement gradient along the line-of-sight of the radar. In other words, the higher the position, the farther the block is from the radar, or the lower the position, the nearer the block is to the radar. This fringe system, which is discussed in the next section, allows us to construct a model.

Discussion

Phase changes due to atmospheric water vapor were observed in all five interferograms; however, those produced by the DEME method (Plates 3d and 3e) appear to be much greater than those produced by the three-pass method (Plates 3a to 3c). Moreover, this difference was also observed in the result of the larger area shown in Plate 2. Without prior knowledge concerning the existence of the landslide, phase variations due to water vapor may be confused with features of the landslide in the interferogram produced by the DEME method. In this case, the local phase variations due to water vapor can be reduced by filtering the interferogram with a larger filter, such as a 25-look by 75-look filter (330-m square); however, some features of the landslide are also lost in this process. Interferograms produced by the three-pass method however are quite clear, especially for the mean phase changes (corresponding to Plate 3a). This is attributed to the equivalent effect of averaging multiple interferograms when applying Equation 4 in the three-pass method. Without prior knowledge concerning the landslide, deformation fringes associated with the landslide can be detected, but the fringe geometry cannot be accurately recovered by the three-pass method.

The interferograms produced by the DEME method indicate the landslide motion is not stationary from June to October, 1995, indicating that the assumption of constant velocity for the three-pass method is invalid. The three-pass method is not suitable for precise measurement of this type of landslide. Even using the DEME method, measurement of small-scale deformation with large displacement and/or heterogeneous motion is difficult. However, if an organized fringe system is observed as in Plate 3e, a slip model can be constructed.

We considered the two most important sliding models:

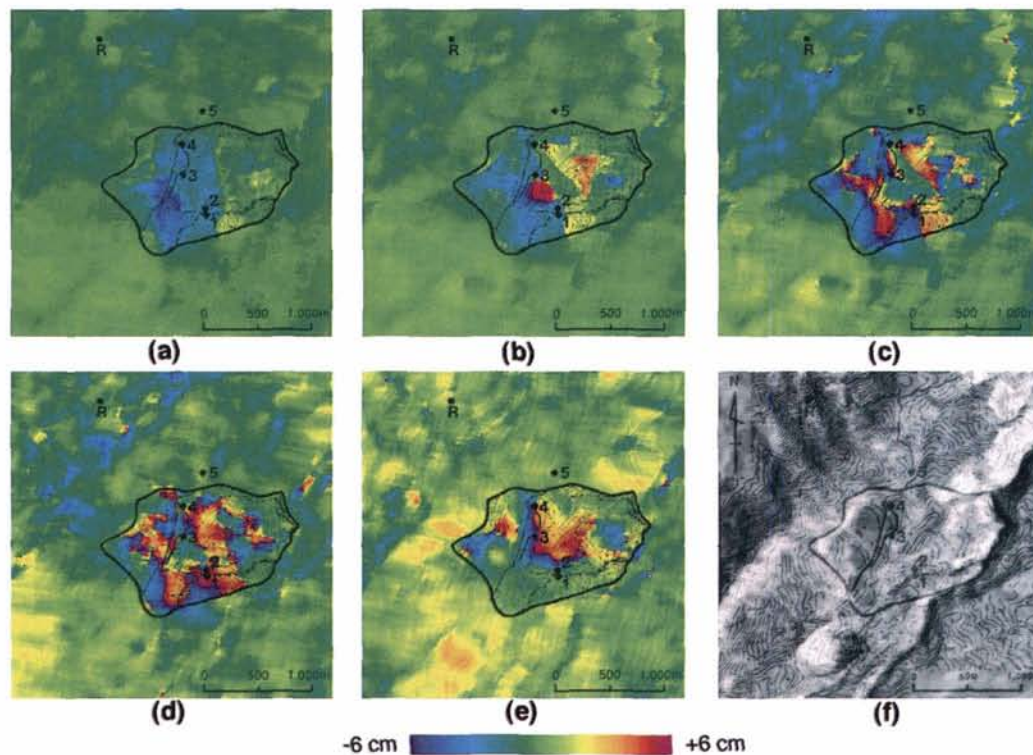


Plate 3. Geocoded differential interferograms and backscatter image. The outline of the landslide block or map is superimposed on each image. Produced by the three-pass method: (a) Average interferogram of an elapsed time of 44 days, (b) Interferogram of an elapsed time of 44 days, from June to September and September to October pairs, (c) Rescaled (b) by a factor of 2, corresponding to an elapsed time of 88 days. Produced by the DEMET method: (d) Interferogram June to September (e) Interferogram September to October (f) Backscatter amplitude.

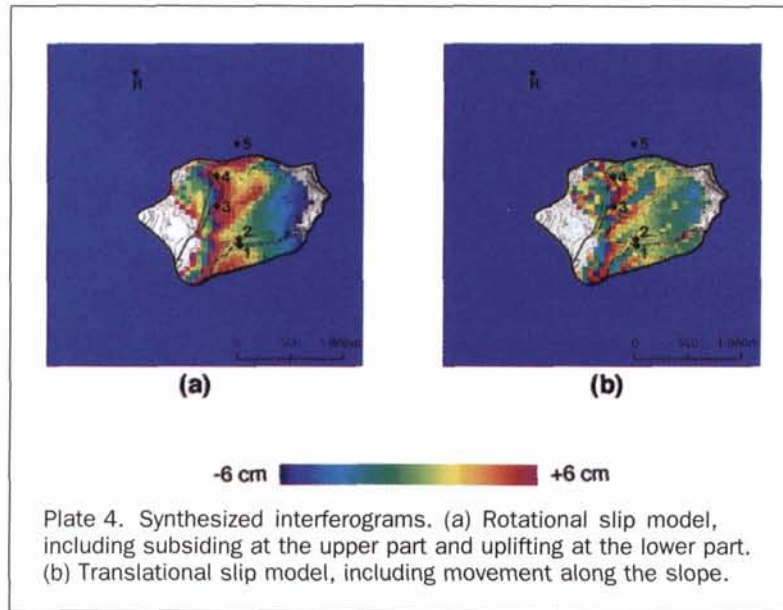
rotational and translational slips. The latter model well describes the St-Etienne-de-Tinee landslide (Fruneau *et al.*, 1996). Based on the fringe systems of the September to October interferogram (Plate 3e), synthetic interferograms were computed for only the areas having a height ranging from 800 m to 940 m, in which the close relationship between phase changes and heights is observed. The phase rotation in Plate 3e indicates that either the vertical motion increases or the eastward motion decreases toward the upper part. Interferograms provide only the gradients of the displacements. This displacement pattern indicates movement of the whole landslide block along an arcuate deep slip plane. More precisely, the middle to upper part of a landslide block is subsiding, while the lower part is uplifting. The displacement of a certain position with respect to the surrounding bedrock is arbitrarily set to zero. In the rotational slip model, the displacement field-including subsiding in the upper part, uplifting in the lower part, and no displacement at a height of 870 m- is assumed (Plate 4a). In the translational slip model, the displacement field-including a slip parallel to the slope, increasing displacement rate toward the lower part, and no displacement at a height of 930 m- is assumed (Plate 4b). The relationship between height and displacement (Table 3) was introduced to further improve the fit between observed and synthetic fringes at the upper part (around 940 m) and the lower part (around 820 m).

Plate 4a, which is derived from the rotational model, shows a satisfactory agreement with Plate 3e in the central part of the landslide. However, Plate 4b, which is derived from the translational model, is not consistent with Plate 3e.

The fringes in Plate 4b suggest a relationship to the direction of the local slope rather than to the height. This suggests that the deformation from September to October is related to rotational slip.

The discrepancy between the June-to-September and September-to-October interferograms (Plates 3d and 3e) suggests that the mechanical behavior is different between these two periods and that the landslide is partitioned into several sub-blocks. The interferograms and the precipitation record (Figure 2) allow us to form the following model of the Itaya landslide. From June to September, the ground water level is generally high due to increased precipitation. As a result, sub-block movements along shallow slip planes are active. From September to October, the sub-block movements are relatively inactive due to decreased precipitation. As a result, the steady-state movement of the entire landslide block along the deep arcuate slip plane is observed. This steady-state movement should occur throughout the year, but is unclear from June to September, because the sub-block movements dominate the steady-state movement of the entire block.

The GPS measurements of 1996 (Table 1) did not provide enough data to construct a detailed landslide movement model, as shown above. This is due to a lack of enough GPS measurements and to the difference in time. According to the model, subsidence near points #3 and #4 reaches 8 cm over 44 days, or 0.2 cm/day. Actually, subsidence is observed as shown in Plate 1b. Therefore, the September-to-October interferogram seems to reveal the specific state of the landslide, indicating an advantage of SAR interferometry.



Conclusions

JERS-1 SAR interferometry was demonstrated as being capable of detecting landslides. Both the three-pass and DEME methods were applied. With the three-pass method, a part of or most of the landslide can be separated from the surrounding areas as phase anomalies, without prior knowledge of the landslide's existence. However, the three-pass method is not suitable for detecting the detailed features of a landslide having large displacement and unsteady-state movement. Interferograms produced by the DEME method show different fringe systems between the June-to-September and the September-to-October periods, allowing the different mechanical behaviors of the landslide during these periods to be considered, and suggesting the presence of several small sub-blocks within the major landslide block. The displacement pattern that includes subsiding in the upper part and uplifting in the lower part based on the rotational slip model, satisfactorily, accounts for the central part of the landslide in the September to October interferogram. These interferograms allow us to construct the model of active movements of sub-blocks along shallow slip planes during the larger precipitation period, and the steady-state movement of the whole landslide block along the deep arcuate slip plane during the lower precipitation period. SAR interferometry can be used to reveal behavior of a landslide that may not have been known before. A shorter observation period would improve the accuracy of the determination of the displacement.

This study provides a preliminary model of the Itaya landslide, especially for the central part, in which GPS points #3 and #4 are located. A different model will describe the behavior of the southwestern part, in which GPS points #1 and #2 are located. Further observations of the landslide are necessary in

TABLE 3. RELATIONSHIP BETWEEN HEIGHT AND DISPLACEMENT FROM A CERTAIN OFFSET USED TO PRODUCE THE SYNTHETIC INTERFEROGRAMS

Height (m)	Vertical motion (cm)	Slip Parallel to Slope (cm)
	Plate 4a	Plate 4b
800	+7.8	+27.5
870	0	+18.3
920	-7.8	+9.2
930	-15.6	0
940	-23.4	-9.2

order to construct a precise model of the entire landslide. A rapid phase change associated with deformation over small areas makes it difficult to identify areas having no displacement. In addition, ground measurements are necessary in order to recover the absolute displacement to complement interferogram analysis. Although the number of ground measurement points will likely be limited as in the present case, interferograms will offer useful information for deployment of ground instruments.

Acknowledgments

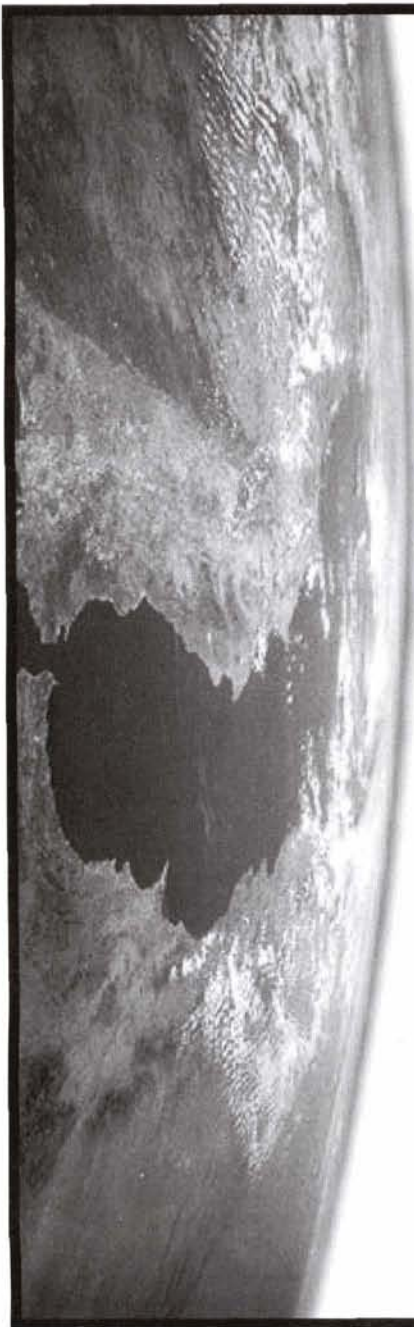
The authors would like to thank the reviewers for their valuable comments and suggestions, which have improved the content and quality of the manuscript. The authors would also like to thank to Toshitaka Kamai for providing the information on the Itaya landslide and Naohiro Yamada for his contributions to the phase unwrapping procedure. All JERS-1 SAR data used in this paper was provided under the JERS-1 Research Invitation Program by the National Space Development Agency of Japan (NASDA). The Ministry of International Trade and Industry (MITI) and NASDA retain ownership of the original JERS-1 SAR data.

References

- Carnec, C., D. Massonnet, and C. King, 1996. Two examples of the use of SAR interferometry on displacement fields of small spatial extent, *Geophys. Res. Lett.*, 23(24):3579-3852.
- Curlander, J., and R. McDonough, 1991. *Synthetic Aperture Radar*, John Wiley & Sons, New York, pp. 437-452.
- Fruneau, B., J. Achache, and C. Delacourt, 1996. Observation and modelling of the Saint-Etienne-de-Tinee landslide using SAR interferometry, *Tectonophysics*, 265:181-190.
- Fujii, N., S. Kobayashi, A. Mio, Y. Yamaguchi, R. Miyajima, T. Okuda, and F. Kimata, 1997. Precise detection of rapid volcanic deformations: Combination of dense GPS and D-InSAR (ex: flank of Azuma Volcano), *Abstracts of the Fall Meeting of the Volcanological Society of Japan*, p. 84 (in Japanese).
- Fujiwara, S., P. Rosen, M. Tobita, and M. Murakami, 1998. Crustal deformation measurements using repeat-pass JERS1 synthetic aperture radar interferometry near the Izu Peninsula, Japan, *J. Geophys. Res.*, 103(B2):2411-2426.
- Gabriel, A., R. Goldstein, and H. Zebker, 1989. Mapping small elevation change over large areas: Differential radar interferometry, *J. Geophys. Res.*, 94(B7):9183-9191.

- Goldstein, R.M., H. Englehardt, B. Kamb, and R.M. Frolich, 1993. Satellite radar interferometry for monitoring ice sheet motion: Application to an Antarctic Ice Stream, *Science*, 262(1):525-1,530.
- Goldstein, R.M., H.A. Zebker, and C.L. Werner, 1988. Satellite radar interferometry: Two-dimensional phase unwrapping, *Radio Science*, 23(4):713-720.
- Joughin, I.R., R. Kwok, and M.A. Fahnestock, 1998. Interferometric estimation of three-dimensional ice-flow using ascending and descending passes, *IEEE Trans. Geosci. Remote Sensing*, 36(1):25-37.
- Kimura, H., and M. Todo, 1997. Baseline estimation using ground points for interferometric SAR, *Proc. 1997 IEEE International Geoscience and Remote Sensing Symposium*, pp. 442-444.
- Kwok, R., and M. A. Fahnestock, 1996. Ice sheet motion and topography from radar interferometry, *IEEE Trans. Geosci. Remote Sensing*, 34(1):189-200.
- Massonnet, M., P. Briole, and A. Arnaud, 1995. Deflation of Mount Etna monitored by spaceborne radar interferometry, *Nature*, 375:567-570.
- Massonnet, M., M. Rossi, C. Carmona, F. Adragna, G. Peltzer, K. Feigl, and T. Rabaute, 1993. The displacement field of the Landers earthquake mapped by radar interferometry, *Nature*, 364:138-142.
- Massonnet, M., H. Vadon, and M. Rossi, 1996. Reduction of the need for phase unwrapping in the radar interferometry, *IEEE Trans. Geosci. Remote Sensing*, 34(2):489-497.
- Yamaguchi, Y., S. Tanaka, T. Odajima, S. Tsuchida, and T. Kamai, 1999. Detection of landslide movement using SPOT HRV and ADEOS AVNIR data in Azumayama Area, Japan, *Proc. Thirteenth International Conference on Applied Geologic Remote Sensing*, 11:97-103.
- Zebker, H.A., P. Rosen, R.M. Goldstein, A. Gabriel, and C.L. Werner, 1994. On the derivation of coseismic fields using differential radar interferometry: The Landers earthquake, *J. Geophys. Res.*, 99(B10):19,617-19,634.

(Received 31 July 1998; revised and accepted 26 April 1999)



PE&RS SPECIAL ISSUE ★ OCTOBER 2000

REMOTE SENSING AND DECISION SUPPORT SYSTEMS

In October 2000, the American Society for Photogrammetry and Remote Sensing will devote its issue of *Photogrammetric Engineering and Remote Sensing (PE&RS)* to Remote Sensing and Decision Support Systems (DSS). DSS would include the science-based predictive models, remote sensing information, verification and validation, and the communities that conduct the decision support. Authors are encouraged to submit manuscripts addressing remote sensing and GIS contributions to operational Decision Support Systems.

Possible categories of manuscripts include Decision Support Systems used for:

- Precision Agriculture (Food and Fiber)
- Coastal Ecosystem Management (Natural Resources)
- Flood Plain Risk Assessment (Disaster Management)
- Water Quality (Environmental Quality)
- Urban Planning (Urban and Infrastructure)
- Public Health (Human Health and Safety)

We also encourage the submission of short manuscripts that present the experience of remote sensing/GIS by Federal, State, or Local agencies using decision support systems operationally. Private sector companies under contract to these agencies or otherwise involved in some aspect of developing or operating decision support systems using remote sensing/GIS technology are also invited to submit a short manuscript.

Guest Editors

Ronald J. Birk, Intermap Technologies Inc.

Dr. Timothy W. Foresman, University of Maryland-Baltimore

All manuscripts must be prepared according to the "Instructions to Authors" published in each issue of *PE&RS*. Papers will be peer-reviewed in accordance with established ASPRS policy. Please send manuscripts to:

Ronald J. Birk

Intermap Technologies Inc.

Bldg. 1110

Stennis Space Center, MS 39529

228.688.1673 (fax)

rbirk@intermaptechnologies.com

DEADLINE

MAY 15, 2000